Reviews
doi.org/10.1002/batt.202000239

Chemistry Europe
European Chemical Societies Publishing

Recent Advances in Stability of Carbon-Based Anodes for Potassium-Ion Batteries

Jiali Wang[+],[a] Huwei Wang[+],[b] Xiaobei Zang,[c] Dengyun Zhai,*[a] and Feiyu Kang*[a, b, d]

doi.org/10.1002/batt.202000239

The commercialization of potassium-ion batteries requires promising anodes with excellent reversible capacity and cycle stability. Graphite anodes have attracted extensive research owing to the formation of stable intercalation compounds, which also helps to focus attention on low-cost carbon-based anodes. However, the slow diffusion of potassium ion (K^+) and structural damage of graphite caused by large size may lead to capacity decay. Herein, the modification strategies have been summarized, including microstructure regulation, heteroatom doping and building stable solid electrolyte interphase. And the opportunities and challenges faced by these improvement methods are proposed. Meanwhile, carbon-based materials used as hosts or conductive carriers to improve the performance of other anodes are also summarized.

1. Introduction

With the exhaustion of traditional energy sources, the development of renewable energy technologies has become a general trend. However, renewable energy supply such as wind, solar and hydropower is often intermittent.[1] Thus the development of large-scale energy storage systems becomes the key to the popularization and application of renewable energy.[2] Owing to the long cycle life and high energy density, lithium ion batteries (LIBs) become superior energy storage devices.[3] However, the lithium resource in the earth's crust is only 0.0017 weight %, and it is estimated that LIBs have consumed 20% of global lithium production.[4] Besides, the uneven distribution of lithium is unable to meet the demand for stationary energy storage.[5] To address those issues, the alternative batteries based on the more abundant alkali metal elements have been exploited, such as sodium (2.32 weight %) and potassium (1.68 weight %).[5–6] Unfortunately, graphite, the commercial anode materials for LIBs, cannot host intercalated sodium ion, thus limiting the application of sodium ion batteries.[7] Although the solvated sodium ions with solvent molecules can co-intercalate into graphite in some specific electrolytes, the graphite delivered a low capacity of 35 mAh/g by forming NaC_{64} during sodiation.[8] Meanwhile, the high intercalation potential leads to the low energy density of the full cell.[9] In contrast, the advantages of potassium-ion batteries (KIBs) are prominent as follows. 1) The standard electrode potential of K/K^+ (−2.93 V versus E^0) is close to Li/Li^+ (−3.04 V versus E^0), providing a wide voltage window for KIBs.[10] 2) The Lewis acidity of K^+ ion is weak with the small Stoke radius, rendering the rapid ion diffusion of K electrolytes.[11] 3) K^+ ions can reversibly intercalate/de-intercalate from graphite, thus low-cost graphite as anode could be used in KIBs.[12]

Although KIBs have many outstanding merits, they are still in infancy due to the lack of suitable anodes. Nowadays, many types of anodes have been investigated, such as graphite, graphene, alloys, metal sulfides and so on.[13] Regarding on the commercialization of KIBs, electrode materials have been put forward more stringent requirements, such as stability, non-toxicity and low cost. Among them, only carbon-based anode materials could satisfy all demands, exhibiting great application prospect. Graphite, the successful anode materials for LIBs, has developed complete industrial production process and technology. At present, graphite is the most promising in the KIBs anode, and the current industrialization of LIBs may provide guidance for the commercialization of KIBs. Nevertheless, the intercalation of large K^+ ions (0.138 nm) causes the severe volume expansion (61% upon full potassiation) and even the active materials peel off from the current collector, leading to the poor cycle stability and rate capacity.[15] The graphite anode failed to deliver capacity after 150 cycles in EC:DMC (ethylene: dimethyl carbonate) electrolyte.[16] Consequently, the main difficulty in carbon-based anodes is to find suitable materials with high cycle stability and reversible capacity for KIBs. In the past few years, many strategies have been proposed to fabricate promising anodes.[17] Expanded interlayer space could accommodate more K^+ ions and maintain structural stability, moreover, engineering porous carbon will increase specific surface area to shorten K^+ ions diffusion distance.[18] For example, rGO aerogel with large interlayer space exhibited a better capacity of 208 mAh/g after 100 cycles.[19] Furthermore, defective carbon caused by heteroatom doping could produce more active sites for K^+ ions adsorption, which delivered a capacity higher than the theoretical capacity. [20] Another critical concern is to explore stable electrolytes for carbon-based anodes. The composition of electrolytes determines the stability of solid electrolyte interface, thus affecting the cycle stability and Coulomb efficiency of anodes.[21] Therefore, in order to achieve a breakthrough in properties for KIBs, considerable efforts in electrolyte and additive have been engaged to build robust solid electrolyte interface (SEI).[70]

In this review, a detailed summary of boosting the stability of carbon-based anodes has been discussed, especially from

[a] J. Wang,[+] Prof. D. Zhai, F. Kang
Advanced Materials Institute,
Graduate School at Shenzhen
Tsinghua University
Shenzhen, 518055, China
E-mail: zhaidy0404@sz.tsinghua.edu.cn
[b] H. Wang,[+] F. Kang
Shenzhen Environmental Science and
New Energy Technology Engineering Laboratory
Tsinghua-Berkeley Shenzhen Institute (TBSI)
Tsinghua University
Shenzhen, 518055, China
E-mail: fykang@mail.tsinghua.edu.cn
[c] Prof. X. Zang
School of Materials Science and Engineering
China University of Petroleum (East China)
Qingdao, 266580, China
[d] F. Kang
Shenzhen Key Laboratory for Graphene-Based Materials and
Engineering Laboratory for Functionalized Carbon Materials
Shenzhen Geim Graphene Center,
Tsinghua Shenzhen International Graduate School
Tsinghua University
Shenzhen, 518055, China
[+] These authors contributed equally to this work.

perspectives of microstructure regulating and electrolyte matching (Figure 1). We highlight and amplify the challenges and opportunities of the anodes for KIBs to provide future research areas that are insufficiently explored currently, such as the immature preparation process of expanded graphite, unclear doping mechanism and slow development of electrolyte additives. The carbon-assisted anodes are also contained, including carbon/alloying composite anodes and carbon/conversion composite anodes.

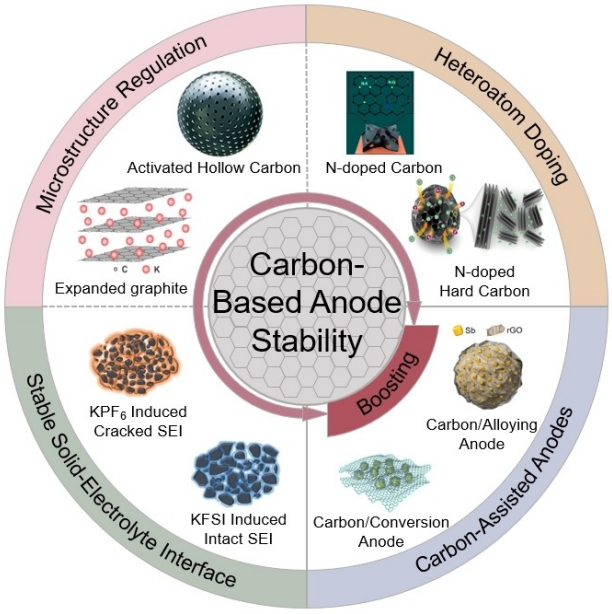

Figure 1. Illustration of strategies to boost the stability of carbon-based anodes and carbon-assisted anodes.

2. Storage Mechanism of KIBs

KIB is a rocking-chair type battery similar to its Li-ion cousin.[7,22] In the charging process, the electrochemically dissolved K^+ ions from the cathode diffuse through the electrolyte and intercalate into the anode (Figure 2a), and the discharging process works in reverse.[8b] Based on different reaction mechanisms, the anode materials for KIBs can be generally divided into intercalation-type, alloy-type and conversion-type.[11a,23]

Carbon-based anode is the most representative among the intercalation-type anode materials, and the graphite anode is taken as an example for discussion as follows. The energy storage process of graphite is achieved by forming potassium graphite intercalation compounds (K-GICs). In 2015, Jian et al. first reported the phase change process of K^+ ions intercalated into graphite via ex situ X-ray diffraction (ex-situ XRD) analysis.[8c] The forming KC_{36} turn to KC_{24} and further shift to KC_8 upon discharging to 0.1 V. However, based on the DFT calculation, Luo et al. reported that the products of K-GICs are KC_{24}, KC_{16} and KC_8, respectively (Figure 2b, c).[24] The DFT

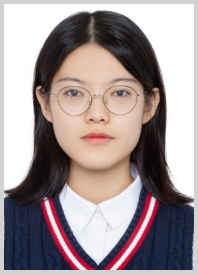

Jiali Wang is currently a M.S. candidate in Tsinghua Shenzhen International Graduate School, Tsinghua University, China. She received her B.S. degree from China University of Petroleum (East China) in 2020. Her current research interests focus on the design of carbon-based anodes for alkali metal-ion batteries.

Huwei Wang is a Ph.D. candidate in Tsinghua-Berkeley Shenzhen Institute (TBSI), Tsinghua University, China. He received his B.S. degree from Northwestern Polytechnical University in 2016. His current research interests focus on the electrolyte design and the interface of alkali metal-ion batteries.

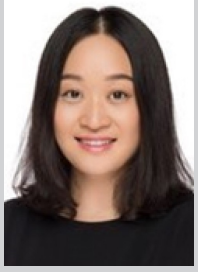

Xiaobei Zang is currently an Assistant Professor at China University of Petroleum (East China). She received her Ph.D. in the school of Materials Science and Engineering, Tsinghua University, China, and received her B.S. degree (2007) and M.S. degree (2010) from the College of Mechanical and Electronic Engineering, China University of Petroleum (East China). Her research interests focus on nanocarbon materials-based electrode materials for flexible energy storage devices.

Dengyun Zhai is an associate professor at Tsinghua Shenzhen International Graduate School, Tsinghua University. He received his Ph.D. in 2011 from Tsinghua University, China. His research interests focus on the design of carbon materials and their applications in energy storage devices such as alkali metal-air batteries and ion batteries.

Feiyu Kang was born in 1962, received doctoral degree from Hong Kong University of Science and Technology. He now is a full professor in Department of Materials Science and Engineering, Tsinghua University. His research is focusing on nanocarbon materials, graphite, thermal conductive materials, lithium ion battery, super-capacitors, electric vehicles, porous carbon and adsorption, indoor air clearing and water purification.

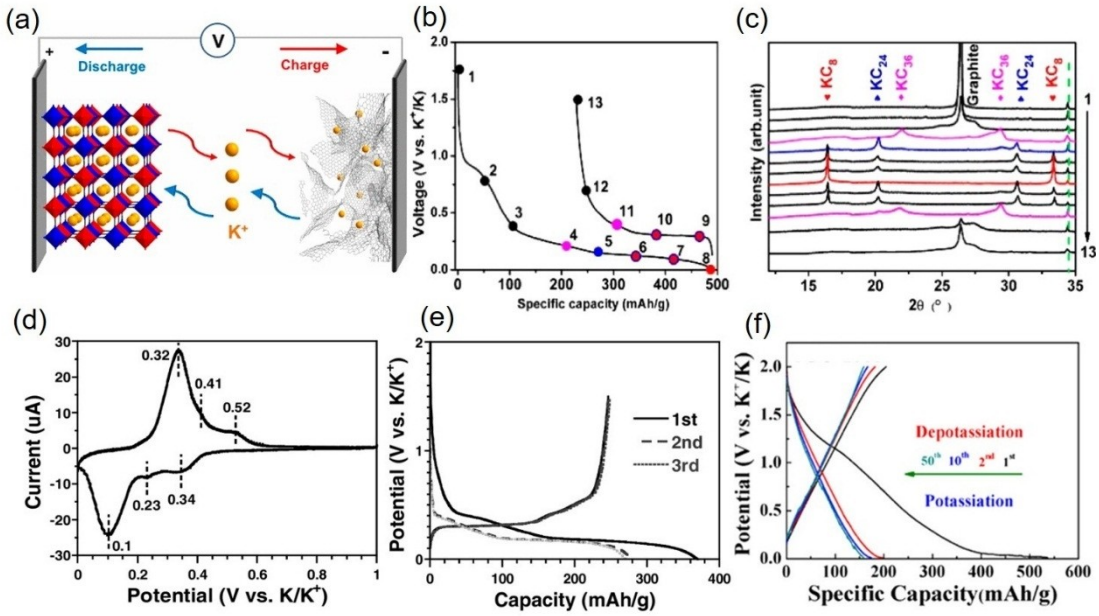

Figure 2. Schematic illustration of potassium storage mechanism. a) The "rocking chair" storage mechanism of K^+.[22] Reproduced from Ref. [22] with permission. Copyright (2017) American Chemical Society. b) First cycle GCD curves of K-GICs and c) ex situ XRD patterns of different points.[8c] Reproduced from Ref. [8c] with permission. Copyright (2015) American Chemical Society. d) CV curve of KIBs with graphite anode. e) GCD curves of KIBs with graphite anode.[16] Reproduced from Ref. [16] with permission. Copyright (2016) Wiley-VCH. f) Slope-like GCD curves for KIBs.[26] Reproduced from Ref. [26] with permission. Copyright (2019) American Chemical Society.

calculation results are inconsistent with the ex situ experimental observation, which may be caused by the decomposition of K-GICs during the disassembly of KIB. Regarding the mechanism of K^+ ions storage in carbon-based anodes, types of electrolyte matters to the intercalation reaction. The binary intercalation dominates in the ester electrolyte and high concentration ether electrolyte, i.e., K^+ ions intercalation occurs without the solvent molecule.[25] However, K^+ ions along with solvation sheath intercalate into graphite in the low concentrated ether electrolyte. Such co-intercalation behavior forms a ternary GICs and the corresponding specific capacity can only reach 110 mAh/g.[26]

Through alloying reaction with potassium, alloy-type anode demonstrates a high theoretical capacity compared with the intercalation-type anode. Many significant advances have been achieved in alloy anode, including antimony (Sb), bismuth (Bi), red phosphorus (P) and so on.[27] K–Sb alloy, a typical example of alloy anode in KIBs, was first reported in 2015.[28] Its alloying reaction process has been proved as follows: the binary phase transition between K and Sb generates four kinds of products, including KSb_2, KSb, K_5Sb_4 and K_3Sb.[29] It is worth noting that there are only two pairs of redox peaks in the cyclic voltammetry (CV) curve due to the close thermodynamic equilibrium potentials of the products.[29]

In addition to alloying/de-alloying, conversion mechanism with high theoretical capacity has also been explored. Especially the transition metal sulfides with lamellar structure have become considered candidates for KIBs.[30] And based on different features, their K storage mechanisms are divided into conversion-alloying and conversion-intercalation. For instance, tin sulfide (SnS_2) anode complies with the former mechanism: the hexagonal SnS_2 is transformed into layered orthorhombic SnS, and then the formed SnS converts into Sn and K_2S, followed by alloying to form the final KSn.[31] Moreover, the reaction between molybdenum sulfide (MoS_2) and K^+ ions consists of intercalation and conversion. That is, the K^+ ions-intercalated product (K_xMoS_2) undergoes conversion reaction to generate Mo and K_2S.[30]

The storage of K^+ ions in carbon-based anodes involves two kinetic processes, i.e, (1) the surface-controlled K^+ adsorption and (2) diffusion-controlled K^+ intercalation.[32] The former is a rapid process, thus it improves the rate performance of anodes. This process mainly depends on the specific surface area of carbon materials. Nevertheless, the latter determines the theoretical capacity of carbon-based anodes. These two processes can be qualitatively analyzed through the CV curve and galvanostatic charging/discharging (GCD) test.[33] Judging from the CV curves, the diffusion-controlled storage process will appear pairs of redox peaks corresponding to different reaction products, as shown in Figure 2d.[16] In stark contrast, the surface adsorption storage process does not show an obvious peak feature. The storage mechanism mainly involves K^+ ions adsorption in the pores and defect locations. According to the GCD curves, the intercalation process shows a voltage platform related to phase change (Figure 2e), and the capacitance contribution (adsorption process) shows a slope-like feature, as shown in Figure 2f.[26]

In order to understand the mechanism of KIBs, many advanced techniques are developed. Despite the electrochemical methods (CV and GCD) which are used to observe the

kinetic processes of K^+ ions storage, there are many advanced characterization techniques, especially in situ techniques.[34] In situ characterization techniques can capture the change of materials synchronously during the charge/discharge cycles. For example, in situ transmission electron microscope (TEM) is an emerging technology to observe the status of materials during the process of K^+ ions intercalation/deintercalation. It can vividly show the microstructural evolution of electrode materials during the working condition, such as the change of interlayer spacing, the collapse and reorganization of structure.[35] Similar to the characterization of in situ electron microscopy, by use of in situ XRD the structure of crystalline materials can be investigated via monitoring the change of diffraction degree during the charge/discharge cycle.[36] In the early 2009, Key et al. used Real-time ^{7}Li NMR technology study the local structural changes of silicon electrodes in LIBs to explain the storage mechanism.[37] Therefore, due to the similar energy storage mechanism of the two systems, many advanced technologies related to LIBs could be applied in KIBs.

3. Carbon-Based Anodes

3.1. Graphite Anode

Contributed to the tremendous resources of carbon and high stability of lithium intercalation compound, graphite has become the main anode material for commercial LIBs.[8b,38] Compared with other carbonaceous materials, graphite is environmental friendliness with low voltage platform, making it become the best candidate for anode material. K-GICs as the important structure of potassium storage, have been extensively studied.[39] In the 1960s, researchers have achieved the intercalation of potassium vapor in graphite via physical heating.[40] By controlling the heat treatment temperature, K-GICs with different stages have been achieved. Moreover, with the decrease in temperature (555 to 318 °C), the unsaturation of K-GICs was increased from graphite to KC_8.[40] In 2015, the electrochemically obtained K-GICs delivered a capacity of 273 mAh/g under low current (0.025 C), close to the theoretical capacity of KC_8 (279 mAh/g).[8c] However, the capacity of graphite anode decreased significantly from 197 to 100 mAh/g at C/2 after 50 cycles (Figure 3a).[8c] Furthermore, the volume expansion rate of K^+ ions intercalation is as high as 59.7% compared with LiC_6 (10%). This is because the large K^+ ions could damage the structure of graphite after multiple intercalation/extraction, resulting in poor rate performance (Figure 3b) and low cycle stability.

3.2. Non-Graphite Anodes

Non-graphite carbon is a carbon material with both graphite microcrystalline and amorphous structures, including soft carbon and hard carbon. And soft carbon is subjected to graphitization, achieving the excellent electronic conductivity and rate performance. Jian et al. prepared soft carbon with larger interlayer spacing (0.335 nm) by pyrolysis of 3,4,9,10-perylene tetracarboxylic dianhydride (PTCDA) at 900 °C to explore the effect of interlayer distance on K^+ ion storage performance.[8c] This soft carbon still maintained a capacity of 140 mAh/g even at 5 C (1395 mA/g).[8c] Because of the flexible structure of soft carbon, the storage reaction of K^+ ions in curved carbon layer can be controlled by adjusting the crystallinity to meet the requirements for structural stability and rapid transfer of K^+ ions. Liu et al. carbonized pitch

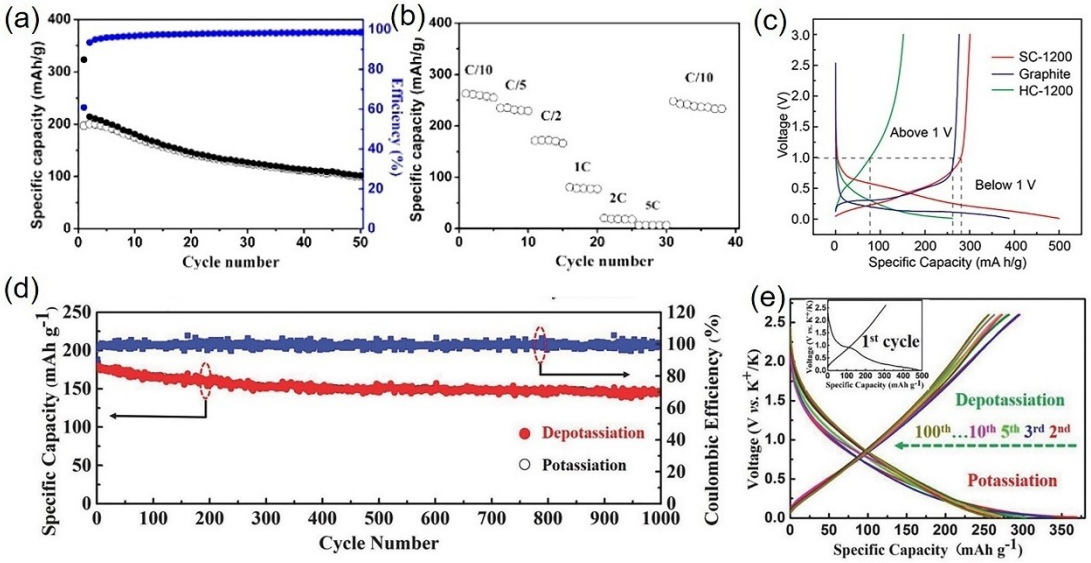

Figure 3. Electrochemical performance of carbon-based anode. a) The cycle performance of graphite anode at 0.5 C. b) The rate capacity of graphite anode at different current density.[8c] Reproduced from Ref. [8c] with permission. Copyright (2015) American Chemical Society. c) The first GCD curves of soft carbon, hard carbon and graphite at 0.1 C.[41] Reproduced from Ref. [41] with permission. Copyright (2020) Wiley-VCH. d) Long cycle stability of hard carbon at 1 A/g after 1000 times. e) GCD curves of sucrose pyrolysis hard carbon at 0.05 A/g.[44] Reproduced from Ref. [44] with permission. Copyright (2018) Wiley-VCH.

precursor at high temperature under nitrogen atmosphere and studied the effect of carbonization temperature on structure and energy storage mechanism.[41] The lattice structure of soft carbon is very sensitive to the heat treatment temperature. The crystallinity was increased with the rise of temperature, leading to the transition of storage kinetics from adsorption to intercalation. The corresponding GCD curve changed from "slope" to "plateau", thus the reversible capacity mainly derived from the low-voltage area (1 V), which was favorable for improving the energy density of full KIBs (Figure 3c). By lowering the heat treatment temperature from 1600 to 1200 °C, the soft carbon could form a turbulent curved carbon layer with large interlayer spacing. And the curved carbon layer reduces the formation of KC_{24} that requires long-range order structure. For instance, the K^+ ions intercalation of SC-1200 (pyrolysis soft carbon at 1200 °C) is continuous without intermediate products, which could make the soft carbon have structural elasticity against mechanical deformation.[41]

Besides soft carbon, hard carbon materials are also common non-graphite carbon materials, which are difficult to be graphitized.[42] Owing to the special disordered and non-expandable stable structural framework, hard carbon can ensure a long cycle life for K^+ ions storage. Chen et al. prepared hard carbon by pyrolyzing pepper,[43] and found that as the pyrolysis temperature increased, the specific surface area and interlayer spacing gradually decreased, but short-range ordered graphite crystallites appeared in hard carbon to form transfer channels of K^+ ions. The excellent cycle performance with 70% capacity retention after 300 cycles was obtained under 0.5 C current test condition.[43] There are many types of hard carbon materials with rich pore structures and large specific surface area, such as mesoporous carbon and microporous carbon. Another carbon source-sucrose has been used to fabricate a short-range ordered mesoporous carbon by template method. Unlike crystallized graphite, this mesoporous carbon possesses large average interlayer spacing (0.521 nm) and fewer carbon atoms in a carbon layer cluster.[44] Even the disordered carbon transformed to partial graphitic stacking after potassiation and the interlayer distance changes to 0.453 nm, which is still larger than K^+ ions.[44] After 1000 cycles at high current density (1 A/g), the mesoporous carbon remained a relatively high capacity at 146.5 mAh/g (Figure 3d). The slope-like curve (Figure 3e) has been explained as follows.[44] 1) The slope-like feature is caused by homogeneous chemical reactions, such as surface adsorption. When the specific surface area of carbon materials is high, a large amount of K^+ ions will be adsorbed on the surface. 2) Due to the large size of K^+ ions, the sluggish intercalation reaction kinetics inhibits the heterogeneous reaction, leading to "slope" feature.

In a word, although the current carbon-based anode has great potential, there are still many shortcomings. Graphite anode for KIBs has a considerable reversible capacity but it suffers from the poor rate performance and cycle stability. Its limited interlayer spacing impedes the insertion of large K^+ ions. The irreversible volume change and the damage of the layered structure of graphite after repeated cycles could cause severe deterioration of cycle performance. Meanwhile, the slow solid-state diffusion in graphite causes poor rate performance. As for the soft carbon with superior rate performance, its low crystallinity and unstable structure deteriorate the cyclability. In addition, although hard carbon displays great cycle stability compared with soft carbon, its relatively low electronic conductivity limits the improvement of its rate performance.

4. Modification Strategies of Carbon-Based Anode

4.1. Microstructure Regulation

Controlling the microstructure of carbon materials, including increasing the interlayer spacing and introducing pore structures, has been widely used to improve the alkali metal ion storage performance of carbon-based anode.[7] In the sodium ion batteries, expanded graphite is prepared by partially reducing the oxidized graphite, as shown in Figure 4a.[35] In the preparation process, expanded graphite with long-range orderly structure has been obtained without ultrasonic peeling. The oxygen-containing functional groups expanded the interlayer spacing, but at the same time, they occupied the storage sites of sodium ions and formed a steric hindrance, reducing the diffusion of sodium ions.[35] Therefore, to find the balance between the oxygen content and the interlayer spacing of expanded graphite, controlling the time of reduction heat treatment is a key to optimizing the storage performance. In KIBs, low-cost commercial expanded graphite with 0.387 nm of interlayer distance also significantly improved the cycle stability, but the carbon layer presents a disordered deposition structure, which indicates that the expansion process of the expanded graphite has not been effectively controlled (Figure 4b).[45] In addition, Tai et al. used graphite as the carbon source to undergo KOH etching activation treatment, and the resultant spacing of carbon layers reached 0.358 nm.[46] Therefore, the diffusion coefficient of K^+ ions was increased by 7 times, which realized rapid electron transfer and promoted the penetration of electrolyte (Figure 4c).[46] As an effective strategy for enhancing the electrochemical performance of expanded graphite, the current preparation process is not yet mature, and the interlayer spacing of expanded graphite has not been effectively controlled. Especially in KIBs, expanded graphite with superior stability has not been studied. Compared with graphite, rGO has the natural advantages of larger interlayer spacing.[47] Our group systematically studied the effect of heat treatment temperature on the microstructure of rGO (Figure 4d), proving that increasing the interlayer spacing is beneficial to store more K^+ ions and alleviate the volume change of K-GICs.[26] The rGO-2500 (heat treatment at 2500 °C) delivered high cycle stability as 88.4 mAh/g at 100 mA/g after 2500 cycles.

Meanwhile, some special structures such as hollow or hierarchical pores can significantly improve the potassium storage cycle stability of the carbon-based anode.[48] Different pore structures act as various roles in carbon anodes: micro-

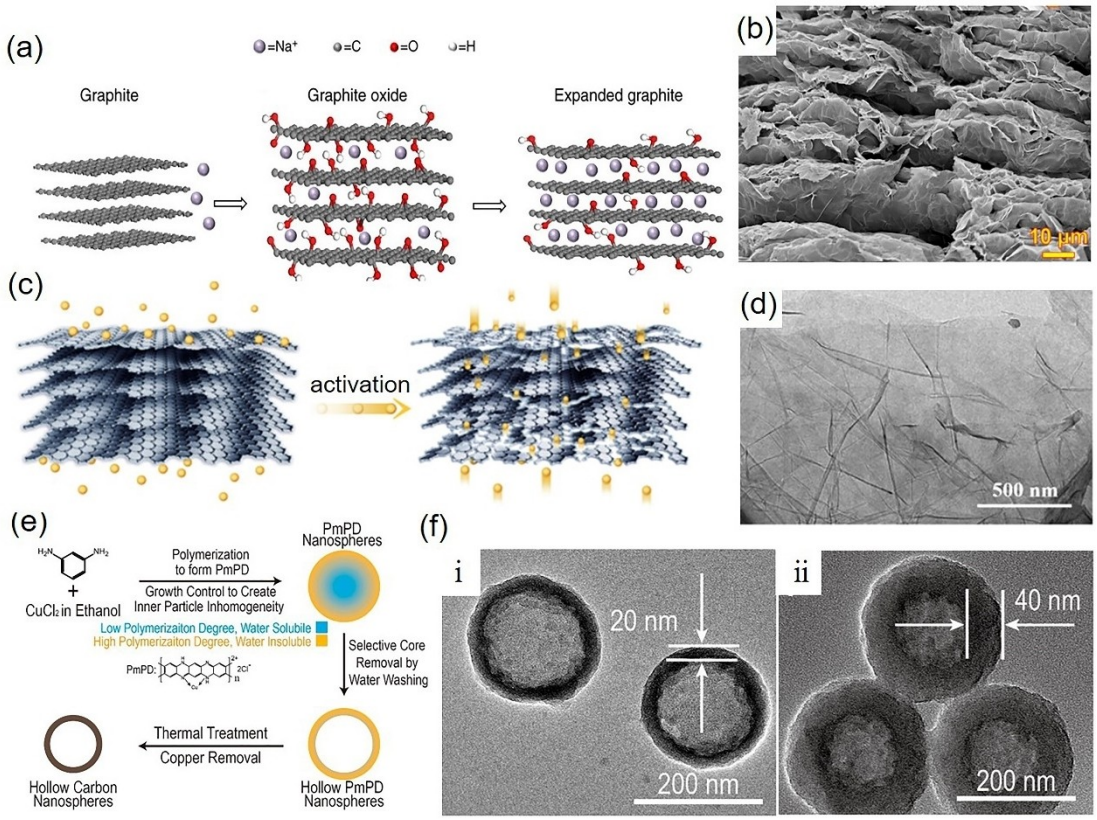

Figure 4. Microstructure regulation strategies. a) Schematic diagram of sodium ion storage performance of graphite, graphene oxide and expanded graphite.[35] Reproduced from Ref. [35] with permission. Copyright (2014) Springer Nature. b) Scanning electron microscope (SEM) image of commercial expanded graphite.[45] Reproduced from Ref. [45] with permission. Copyright (2018) Elsevier. c) Schematic diagram of KOH activated graphite.[46] Reproduced from Ref. [46] with permission. Copyright (2017) Elsevier. d) TEM image of rGO-2500.[26] Reproduced from Ref. [26] with permission. Copyright (2019) American Chemical Society. e) Schematic diagram of polymerization-water washing method. f) TEM image of the hollow carbon sphere reacted for (i) 20 min and (ii) 40 min.[49] Reproduced from Ref. [49] with permission. Copyright (2020) American Chemical Society.

pores can increase the specific surface area of the material, improving the absorption capacity of the anode; mesopores can provide abundant nanochannels, which facilitates the fast diffusion of K^+ ions; macropores can store a small amount of electrolyte to reduce the diffusion distance of K^+ ions. As shown in Figure 4e, Tao et al. proposed a polymerization-water washing method to control the size of the cavity inside the hollow carbon sphere.[49] The growth of precursor and its internal water solubility were regulated by changing the temperature of the polymerization reaction and the concentration of the reactants (Figure 4f). Wu et al. prepared hierarchical porous carbon through the pyrolysis of polyacrylic acid (PPA) by the multiple template method.[48b] The porous carbon with hierarchical pores can be synthesized by controlling the content of Zn particles in the precursor. The performance of this hierarchical porous carbon is shown in Table 1.

Although increasing the specific surface area can facilitate the adsorption of K^+ ions, contributing to the superior rate performance, the increase in the surface area will lead to the accumulation of a large amount of SEI and thus reduce the initial Coulombic efficiency (ICE).

4.2. Heteroatom Doping

Heteroatom doping can control the surface electronic structure of carbon materials and introduce defects or hierarchical pores to shorten the ion diffusion path. Therefore, this strategy is often used to improve the potassium storage performance of carbon materials.[20a,50] The electronegativity of nitrogen (3.04) is higher than that of carbon (2.55), thus the doping of nitrogen into carbon materials can enhance the interaction with cations, such as Li^+ ion and K^+ ion.[50b] Nitrogen doping mainly generates three structures, namely pyrrole nitrogen (N-5), pyridine nitrogen (N-6) and graphite nitrogen (N–Q) (Figure 5a).[51] Figure 5b shows their corresponding X-ray photoelectron spectroscopy (XPS) patterns. Firstly, N-5 and N-6 are the active sites of electrochemical reactions, which can increase the surface-controlled capacitance and diffusion rate of K^+ ions. Secondly, N–Q changes the performance of the electron donor to improve the conductivity of carbon materials by forming bonds with graphite.[51] Thirdly, N-doping enhances the wettability of anodes to ensure that the solid-liquid contact interface is fully utilized.[52] Zheng et al. explained the reason why N-5 and N-6 as active sites help lithium ions to intercalate via N-doped graphite particles.[52] As shown in Figure 5c, N-5 and N-6 form vacancies in the carbon layer. And when the

Table 1. Comparison of carbon-based materials K^+ storage performance.

Materials	Reversible capacity [mAh/g]	Rate performance [mAh/g]	Cycle performance [mAh/g]	ICE [%]	Electrolyte	Mass loading [mg/cm^2]	Ref.
Expanded graphite	263 at 10 mA/g	175 at 200 mA/g	174 at 0.2 A/g after 500 cycles	81.56	1 M KFSI in EC/DEC	~2	[35]
KOH activated graphite	209 at 100 mA/g	30 at 1 A/g	100.3 at 0.2 A/g after 100 cycles	-	0.8 M KPF_6 in EC/DEC	-	[46]
rGO-2500	130 at 100 mA/g	56 at 10 C	88.4 at 0.1 A/g after 2500 cycles	62	0.5 M KPF_6 in DEGDME	~1.2	[26]
Hollow carbon sphere	242 at 28 mA/g	100 at 5 C	220 at 28 mA/g after 100 cycles	–	0.8 M KPF_6 in EC/DEC	–	[49]
Hierarchical porous carbon	211.5 at 50 mA/g	76 at 10 A/g	90.1 at 1 A/g after 1000 cycles	24.1	0.8 M KPF_6 in EC/DEC	0.8~1	[48b]
N/O Co-doping HC	304.6 at 0.1 A/g	178.9 at 5 A/g	189.5 at 1 A/g after 5000 cycles	40.8	0.8 M KPF_6 in EC/DMC	~0.9	[54]
N-doping Carbon Fibers	248 at 25 mA/g	101 at 20 A/g	146 at 2 A/g after 4000 cycles	49	0.8 M KPF_6 in EC/PC	~1.5	[9a]
N-doping SC]	293 at 0.05 A/g	151 at 5 A/g	165 at 1 A/g after 500 cycles	30.9	0.8 M KPF_6 in EC/DEC	~1	[50b]
N-doping porous carbon	316 at 50 mA/g	120 at 21 C	129 at 2 A/g after 20000 cycles	46.21	5 M KFSI in DME	0.8~1	[53b]
N/O Co-doping CNTs	365 at 100 mA/g	231 at 2 A/g	120 at 3 A/g after 2000 cycles	–	0.5 M KPF_6 in EC/DEC	~0.8	[53a]
Graphite	263 at 0.1 C	80 at 1 C	100 at 0.5 C after 50 cycles	57.4	0.8 M KPF_6 in EC/DEC	~2	[8c]
Graphite	279 at C/3	–	255 at C/3 after 2000 cycles	–	KFSI:EMC = 1:2.5 (molar ratio)	1.25	[57]
Graphite	246 at 20 mA/g	–	220 at 20 mA/g after 200 cycles	66.5	1 M KPF_6 in EC/PC	–	[16]
Graphite	201.7 at 25 mA/g	202 at 4.5 C	200 at 25 mA/g after 300 cycles	82.3	2.76 m KFSI in DME-HFE	~8	[25]
Carbon dots@ rGO paper	310 at 100 mA/g	185 at 500 mA/g	244 at 200 mA/g after 840 cycles	44	0.8 M KPF_6-FEC in EC/DMC	-	[61a]
$NiCo_{2.5}S_4$@ rGO	602 at 50 mA/g	402 at 2 A/g	495 at 200 mA/g after 1900 cycles	78	1 M KFSI in EC/PC	~1	[69]

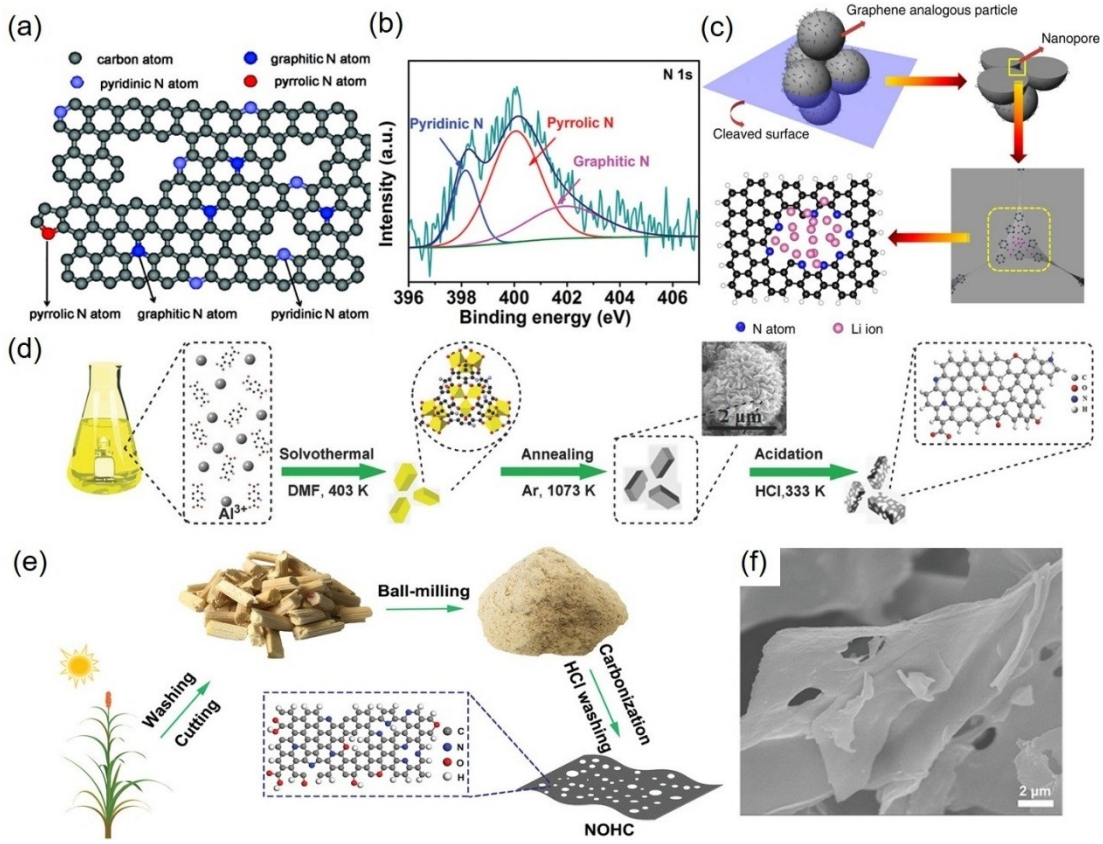

Figure 5. Heteroatom doping. a) Ball and stick model for N-doping carbon.[51] Reproduced from Ref. [51] with permission. Copyright (2011) American Chemical Society. b) XPS pattern for N-doping.[54] Reproduced from Ref. [54] with permission. Copyright (2020) Wiley-VCH. c) Schematic diagram of the storage behavior of lithium ions in nitrogen-doped porous carbon.[52] Reproduced with permission from Ref. [52]. Copyright (2014) Springer Nature. d) Schematic diagram of the preparation process of pyrolyzed MOF structure hard carbon.[32] Reproduced from Ref. [32] with permission. Copyright (2018) Wiley-VCH. e) Schematic diagram of the preparation of sorghum stalks-derived carbon. f) TEM image of sorghum stalks-derived carbon.[54] Reproduced from Ref. [54] with permission. Copyright (2020) Wiley-VCH.

vacancies aggregate, nanopores decorated with N-5 and N-6 will be generated. Those nanopores can adsorb K^+ ions and provide transfer channels for the diffusion of K^+ ions.

There are two strategies for nitrogen doping carbon materials.[52–53] The one is carbonization of carbon-containing raw materials mixed with nitrogen-rich materials (melamine) or under nitrogen-containing gas, such as ammonia or nitrogen. Another is in-situ doping, which is fabricated by high-temperature reduction of precursors containing nitrogen and carbon element framework, such as metal-organic framework (MOF). As shown in Figure 5d, Yang et al. carbonized and acidified an aluminum-based MOF material containing organic ligands of nitrogen and oxygen to obtain N/O co-doping porous hard carbon with increased interlayer spacing (0.39 nm).[32] The special preparation process created hierarchical pore structure of hard carbon. The gas released during the preparation process caused the formation of micropore, and the removal of metal/metal oxide and interstices of particles formed mesopores. At the same time, the macropores are contributed to the layered spacing of the precursor.[32] Such abundant hierarchical pore structures give rise to the high specific surface area (1030 m^2/g), providing sufficient adsorption active sites for K^+ ions. The outstanding electrochemical performance is shown in Table 1. With the increasing awareness of environmental protection, there is a new understanding of the application of biological resources. Cui et al. carbonized renewable sorghum stalks to prepare N/O co-doped hard carbon (Figure 5e, f), forming the increased interlayer spacing in the short-range range, which is favorable for accommodating more K^+ ions.[54] Compared with other methods, this doping method shows the feature of strong operability and lower cost, which is suitable for mass production. The amorphous structure formed by nitrogen doping contains a large number of defects, edges and hierarchical pore structures to provide more active sites, and the hydroxyl groups formed by oxygen doping can improve the wettability of the surface to make full use of the specific surface area. This anode prepared from biological resources retained a high reversible capacity as 304.6 mAh/g at 0.1 A/g after 100 cycles, and even when it is cycled for 5000 times at a large current density of 1 A/g, its reversible capacity also maintained 189.5 mAh/g.[54]

As an important measure to adjust the reaction activity of carbon materials, heteroatom doping is widely used in KIBs. The heteroatoms are doped into the sp^2 hybridized graphene carbon layer to form topological defects and vacancies that can be used as fast channels for ion diffusion and active sites for ion adsorption. Moreover, the doping of heteroatoms on the edges, vacancies, defects, and holes of graphite will change the structure and electronic distribution of graphene. At present, N-doped carbon anode materials for K^+ ion batteries mainly focus on performance research, and the interaction mechanism between doping sites and K^+ ions is still unclear. Besides, the relationship between doping amount and potassium storage performance has not been quantified. As shown in Table 1, compared with the ICE of expanded graphite (81.56%), the modified strategies based on defects is on the premise of sacrificing the ICE, which will lead to more active materials of cathode when matching full cells.

4.3. Building Stable Solid-Electrolyte Interface

The robust SEI formed on the graphite surface will maintain its structural plasticity and ensure good cycle stability. When the SEI layer is unstable, it may be broken under huge stress due to the drastic volume change of electrode materials, exposing the pristine electrode surface without SEI.[55] That will cause the continuous decomposition of the electrolyte, and finally generate a thick SEI film. The destruction/regeneration process of SEI will reduce the Coulombic efficiency. Since the decomposition of the electrolyte will participate in the formation process of SEI, the electrolyte plays a key role in the stability of the anode material. Potassium bis-(fluorosulfonyl)imide (KFSI) has been extensively studied because it has a positive effect on the uniformity, stability and chemical composition of SEI.[53b,56,70] The HOMO (highest occupied molecular orbital) and LUMO (lowest unoccupied molecular orbital) energy levels can be used to understand the thermodynamic stability of the solvents and potassium salts (Figure 6a).[56] The thermodynamic stability window order shows the more reactive feature of KFSI compared with solvents, so the formation of SEI is mainly due to the decomposition of salt. The reduction reaction of salt forms inorganic-rich SEI, which is generally believed to improve the stability of the SEI layer. Furthermore, since the low Lewis acidity of FSI^- leads to the low desolvation energy, KFSI has high ion mobility and low electrolyte impedance.[25] Lu and his co-worker firstly used KFSI-based electrolyte (3 M KFSI in DME) in carbon-based anode for KIBs, which delivered the high reversible capacity of 183 mAh/g after 3000 cycles.[56] Furthermore, Fan et al. used high-concentration KFSI: ethyl methyl carbonate (EMC) (1 : 2.5, mole ratio) electrolyte to form a robust inorganic-rich SEI on the graphite anode, helping to maintain the structural stability during charging/discharging.[57] In the KFSI-based concentrated solution, the formation of SEI mainly occurs at a higher voltage region before the K^+ ion intercalation. As a result, the KFSI-derived stable SEI contributed to achievement of an ultra-long cycle life of over 2000 cycles, as shown in Figure 6b. However, if the voltage exceeds 3.8 V, the typical concentration KFSI-based electrolyte (<1.5 M) will etch the aluminum foil,[58] increasing the salt concentration and purity proved to be effective in addressing this issue.[59] Placke and his co-workers discussed different KFSI-based electrolytes (1 to 4 M) in dual-carbon battery.[60] High concentrated (4 M) KFSI-based electrolyte contains fewer free solvent molecules, thus it cannot dissolve the complexes formed by Al^{3+} and FSI^-, which contributes to the stability of aluminum foil. In order to improve the ionic conductivity of the high-concentration ether electrolyte, Qin et al. prepared a local high-concentration electrolyte by adding highly fluorinated ether (HFE) to the KFSI/DME electrolyte at a specific concentration.[25] This electrolyte enables the graphite anode to form a stable SEI, and the special solvation structure of K^+ ions guarantees its highly reversible intercalation/extraction without significant changes in the

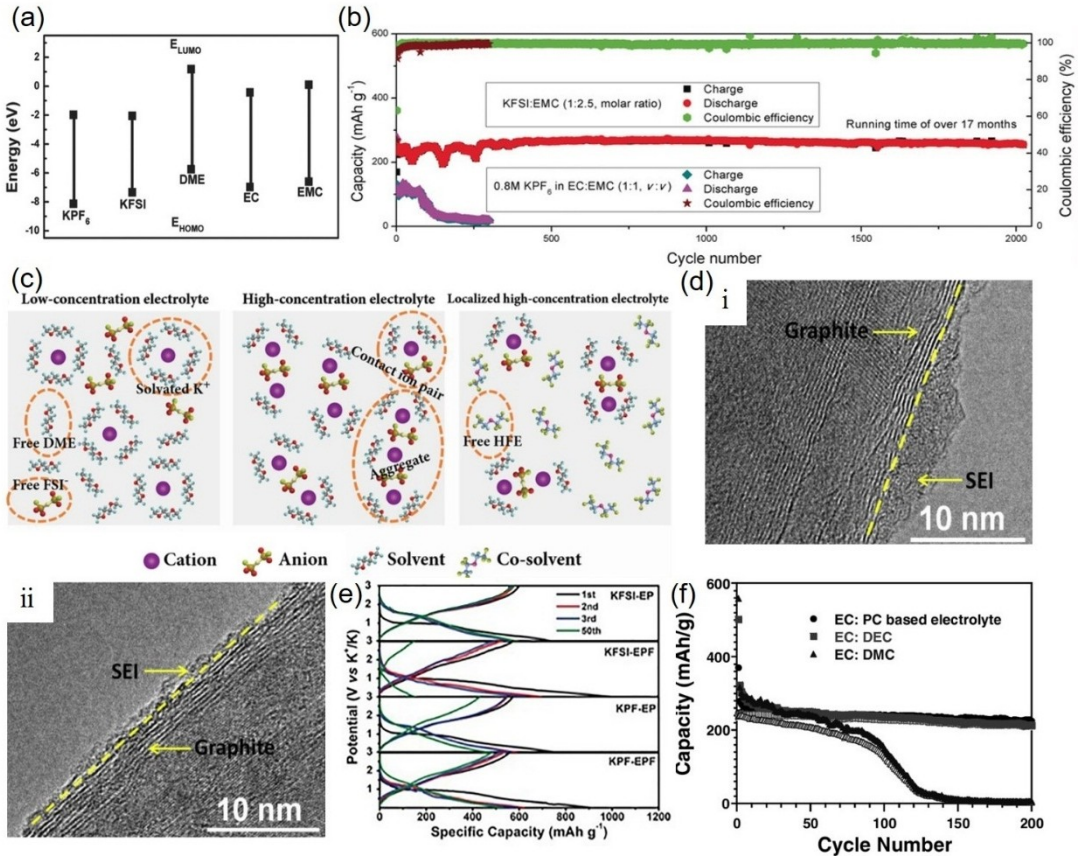

Figure 6. Building stable solid–electrolyte interface. a) The thermodynamic stability window of potassium salts and solvents.[56] Reproduced from Ref. [56] with permission. Copyright (2018) Wiley-VCH. b) Cycle performance of graphite anode in different electrolytes at C/3.[57] Reproduced with permission from Ref. [57]. Copyright 2019 Wiley-VCH. c) Schematic illustrations of solution structures in different electrolyte.[25] Reproduced from Ref. [25] with permission. Copyright (2019) Wiley-VCH. d) TEM images of graphite anode after discharge in (i) EC/DEC and (ii) DEGDME.[21] Reproduced from Ref. [21] with permission. Copyright (2020) Elsevier. e) GCD curves of composites anode using KFSI-EP, KFSI- EPF, KPF-EP, KPF-EPF, where EP is EC:PC, EPF is EC:PC-FEC, KPF is KPF_6.[69] Reproduced from Ref. [69] with permission. Copyright (2019) Wiley-VCH. f) Comparison of cycle performance of graphite anodes in different electrolytes.[16] Reproduced from Ref. [16] with permission. Copyright (2016) Wiley-VCH.

interlayer spacing (Figure 6c). The graphite anode remains highly reversible specific capacity, and even the ICE is 82.3%. Another commonly used potassium salt for anodes, potassium hexafluorophosphate (KPF_6), has a high decomposition voltage in a low-concentration ester electrolyte, but KPF_6-based electrolyte is reduced by solvent-induced reduction to form an unstable organic-dominant SEI.[61,70] Wang et al. compared the different salt-induced SEI layers (KFSI and KPF_6) and found that KPF_6-induced SEI mainly contained unstable alkyl carbonates, which is rough and ruptured.[62] In KPF_6-based electrolyte, PF_6^- is subject to diffuse into graphite layer compared with large FSI^-, leading to the larger mechanical stress of SEI. And the KPF_6-containing electrolyte will continue to decompose in subsequent cycles to repair the broken SEI, resulting in the poor cycle stability of graphite anode.[62] Therefore, KFSI is more superior than KPF_6 for carbon-based anode to ensure the high reversibility.

The stability of the solvent plays a decisive role in the composition of the SEI.[34,63,70] Our group used 0.5 M KPF_6 carbonate/diethyl carbonate (EC/DEC) and diethylene glycol dimethyl ether (DEGDME) electrolytes to study the effect of SEI on capacity decay.[21] The organic SEI on the graphite anode is unstable (Figure 6d), leading to the continuous decomposition of the EC/DEC electrolyte, and the accumulated SEI results in capacity degradation. The decomposition of DEC solvent is caused by the instability of linear DEC molecules, which is contributed to the cleavage of C–O in the solvent molecules.[64] And the compositions of SEI on graphite anode in DEGDME are mainly KF and organic species containing K–O bond.[64] The SEI is more simple compared with reduction products of EC/DEC (unstable alkyl carbonates upon long cycling), indicating the higher stability of DEGDME for graphite.[21,62] DEC and dimethyl carbonate (DMC) both decompose severely, reducing the Coulomb efficiency and leading to poor cycle stability. [16] By contrast, EC/propylene carbonate (PC) electrolyte for graphite anode maintained 220 mAh/g after 200 cycles, which delivered better electrochemical stability (Figure 6e).[16]

With the support of additives, optimizing the electrolyte to build a stable SEI is a convenient strategy to enhance the stability of KIBs. Fluoroethylene carbonates (FEC) additive helps building a stable SEI on the surface of electrode to improve the cycle performance of the LIBs. For example, FEC was reported as the film-forming additives to promote the formation of LiF on the Li anode, which is favorable to enhance the SEI

passivation.[65] In KIBs, Komaba et al. have proved that FEC additive can restrain side reaction of electrolyte for cathode (Prussian blue analogues-PB), enhancing its ICE from 61% to 90%.[66] Later on, Chen et al. proposed that the main effect of FEC in the K/PB cell was on the potassium metal anode to suppress the side reaction of the electrolyte.[67] However, our group also evidenced that the FEC-induced robust SEI on the K metal may lead to the increasing polarization during plating/stripping and further voltage fading.[68] Considering that the K metal is the reference and counter electrode of half-cell, the interfacial reaction of K metal induced the high interface impedance and the increasing polarization, thus affecting the poor electrochemical performance of carbon-based materials. The result also demonstrated that when FEC was used to be an additive for graphite anode, its specific capacity and cycle stability become worse.[66] Xie et al. used FEC additive in the anode for KIBs and found that a thicker SEI was formed, which contributed to a decrease in Coulomb efficiency and an increase in electrode impedance.[69] The addition of FEC will reduce the cycle stability of the anode (Figure 6f). Therefore, FEC may be not suitable to boost the performance of carbon-based anodes for KIBs. In addition, to avoid the side reaction in K metal and explore the mechanism effect of FEC in carbon-based anode, it is necessary to test in full cell.[70]

At present, there are still many problems in the screening of electrolytes. High-concentration electrolyte has high cost and high viscosity, which makes it difficult to wet the electrode. Although high-concentration ether electrolyte achieves binary intercalation, the high cost hinders its further large-scale application. Graphite anode in low-concentration ether electrolytes has low theoretical capacity due to the co-intercalation of solvents. In addition, the instability of the solvent in ester electrolyte has not been solved. Therefore, the development of effective electrolyte additives to solve these problems is urgently needed.

5. Carbon-Assisted Anode

5.1. Carbon/Alloying Anode Material Composites

Since a structural unit of alloy anode can transfer several electrons, the theoretical capacity is extremely high.[10,71] However, serious volume changes during cycles may lead to poor contact between the active materials and the current collector. For example, K_3Sb generated by alloying reaction delivered a theoretical capacity of 660 mAh/g, but its volume expansion rate is as high as 456%.[55] Due to the huge specific surface area and excellent conductivity of carbon-based materials, they not only act as conductive carriers for alloy particles but also play a role as buffering matrix to relieve the mechanical stress of SEI and accommodate volume expansion. Thus, the combination of alloy anode materials and carbon materials is an effective strategy to improve structural stability.[23a,72] Zheng et al. manufactured Sb/carbon nanosphere composites with fine Sb nanoparticles wrapped in the carbon sphere via electrospray and heat treatment.[29] The carbon nanosphere network not only acts as a buffer structure to reduce mechanical damage caused by volume changes, but also is a conductive network to guarantee fast electron transfer. After being composited with carbon materials, the cycle stability was significantly boosted, that is, the reversible capacity still retained 504 mAh/g at 200 mA/g after 220 cycles.[29] Red phosphorus owns a high theoretical capacity of 1154 mAh/g after alloying to form K_4P_3. Red phosphorus has strong chemical stability, but the volume change during the cycle may cause red phosphorus to be crushed. At the same time, the conductivity of red phosphorus is poor, thus the capacity attenuates sharply under fast charge and discharge conditions. Wu et al. coated red phosphorus nanoparticles onto N-doped porous hollow carbon fibers by electrospinning (Figure 7a).[15a] The carbon fiber provided enough space to accommodate the volume change of the red phosphorus. Therefore, the incorporation of carbon fiber improves the stability of the whole structure of the materials. The large specific surface area (2345 m^2/g) derived from the KOH activation (Figure 7b) and the good conductivity along the fiber contribute to the high rate performance (Figure 7c).

In addition, due to its low melting point and thermal conductivity, Bi has been exploited as the promising alloy anode for KIBs. Zhang et al. anchored Bi nanoparticles on the surface of reduced graphite oxide (rGO) by a simple room temperature dissolution method (Figure 7d).[72] The introduction of rGO not only alleviates the agglomeration problem of Bi nanoparticles but also serves as a good conductor of electrons, providing an effective path for electrons transfer. The network structure formed between the two materials could withstand the dramatic volume change caused by the alloying reaction of Bi nanoparticles (The volume expansion rate of the final alloyed product K_3Bi is 515.23%), leading to the better rate performance (Figure 7e). The composite structure could obtain a reversible capacity up to 309 mAh/g at 100 mA/g, which is close to the theoretical capacity (385 mAh/g) of the final product K_3Bi, as shown in Figure 7f.[72]

5.2. Carbon/Conversion Anode Material Composites

Besides carbon-based materials and alloy materials, conversion-type materials have also emerged as the anode candidate for KIBs.[73] For instance, the electronic conductivity of P anode is poor, introducing trasition metal element will enhance the conductivity,[74] but severe volume changes causing by the storage mechanism and metal particles agglomeration issues hinder their further development. Following the technical routes of the composite to address these issues, conversion-type materials are often incorporated with conductive carbon-based matrix to maintain structural stability.[75] Zhang et al. confined Sn_4P_3 nanoparticles in carbon fiber via electrospinning technique, and the modified anode retained stable capacity of 403.1 mAh/g even after 200 cycles at 50 mA/g.[61d] The porous carbon fiber provided buffering space for volume expansion, preventing the pulverization of anode. Owing to the simple two-dimension structure like graphene, transition metal dichal-

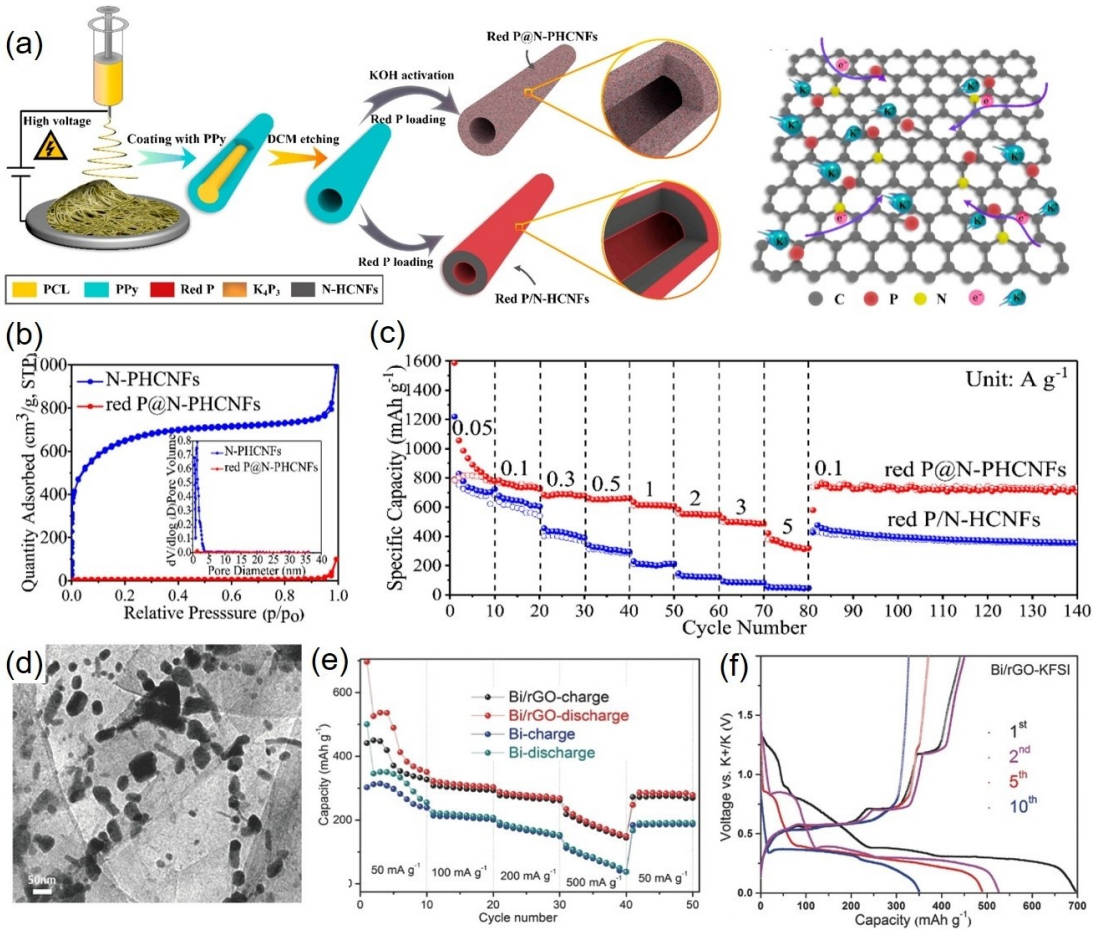

Figure 7. Carbon/alloying anode material composites. a) Schematic diagram of the red phosphorus/carbon fiber by electrospinning method (left) and corresponding structure (right).[15a] b) N_2 adsorption/desorption isotherm of red phosphorus/carbon fiber.[15a] c) Cycle and rate performance of red phosphorus/carbon fiber.[15a] Reproduced from Ref. [15a] with permission. Copyright (2019) American Chemical Society. d) TEM image of Bi/rGO composites; e) Comparison of rate performance between Bi and Bi/rGO. f) Charge and discharge curves of Bi/rGO at 50 mA/g.[72] Reproduced from Ref. [72] with permission. Copyright (2018) Wiley-VCH.

cogenides (TMDCs) have been widely employed recently, such as transition metal selenide and sulfide.[76] Fang et al. synthesized ultra-thin SnS_2 nanosheets vertically arranged on rGO via solvothermal method (Figure 8a, b), which accelerated the diffusion of K^+ ions, increased the active sites and improved conductivity.[31a] The space between the SnS_2 nanosheets can accommodate the volume change during the cycle and inhibit the agglomeration of particles, thus the capacity retention rate after 300 cycles is 73%, as shown in Figure 8c. The content of rGO has a critical effect on the performance of the composite anode. If the content of rGO is too high, the oxygen-containing functional groups in the exposed rGO will irreversibly react with K^+ ions. While the content is too small, the SnS_2 nanoparticles will agglomerate on the rGO surface and lead to the coarsening of Sn grains, reducing the reversibility of the reaction. As a conductive network, rGO is introduced into the nanoflower-like structure MoS_2, as shown in Figure 8d and 8e. The composite of rGO increased the interlayer spacing from 0.615 to 0.637 nm, which benefits to accommodate more K^+ ions intercalation. Furthermore, the specific surface area of the composite increased from 7 to 22.6 m^2/g, forming rich pore structure for electrons transfer and K^+ ions diffusion.[77] The reversible capacity of 438.5 mAh/g has been achieved at 100 mA/g, and the capacity retention rate of 200 cycles was still 95%.

Contributed to the synergistic effect of different metal elements, bimetallic compounds have more electrode reactions and active sites, leading to higher theoretical capacity. Wang et al. prepared Sb_2MoO_6/rGO composite by hydrothermal method reaching a capacity of 402 mAh/g at 100 mA/g, where rGO was a conductive framework to enhance the conductivity of anode.[75b] The formation process of rGO induced the growth of Sb_2MoO_6 and inhibited the agglomeration of nanolayers. This bimetallic composite mainly stores K^+ ions through the conversion and alloying reaction of Sb element, while Mo element acts as a buffer framework to improve the conductivity and stability of anode without capacity contribution.

Overall, the alloying anode and conversion anode materials with high theoretical capacity will produce serious volume expansion during the charging/discharging process, leading to rapid capacity fading. The low-dimensional carbon-based materials with superior electrical conductivity and mechanical

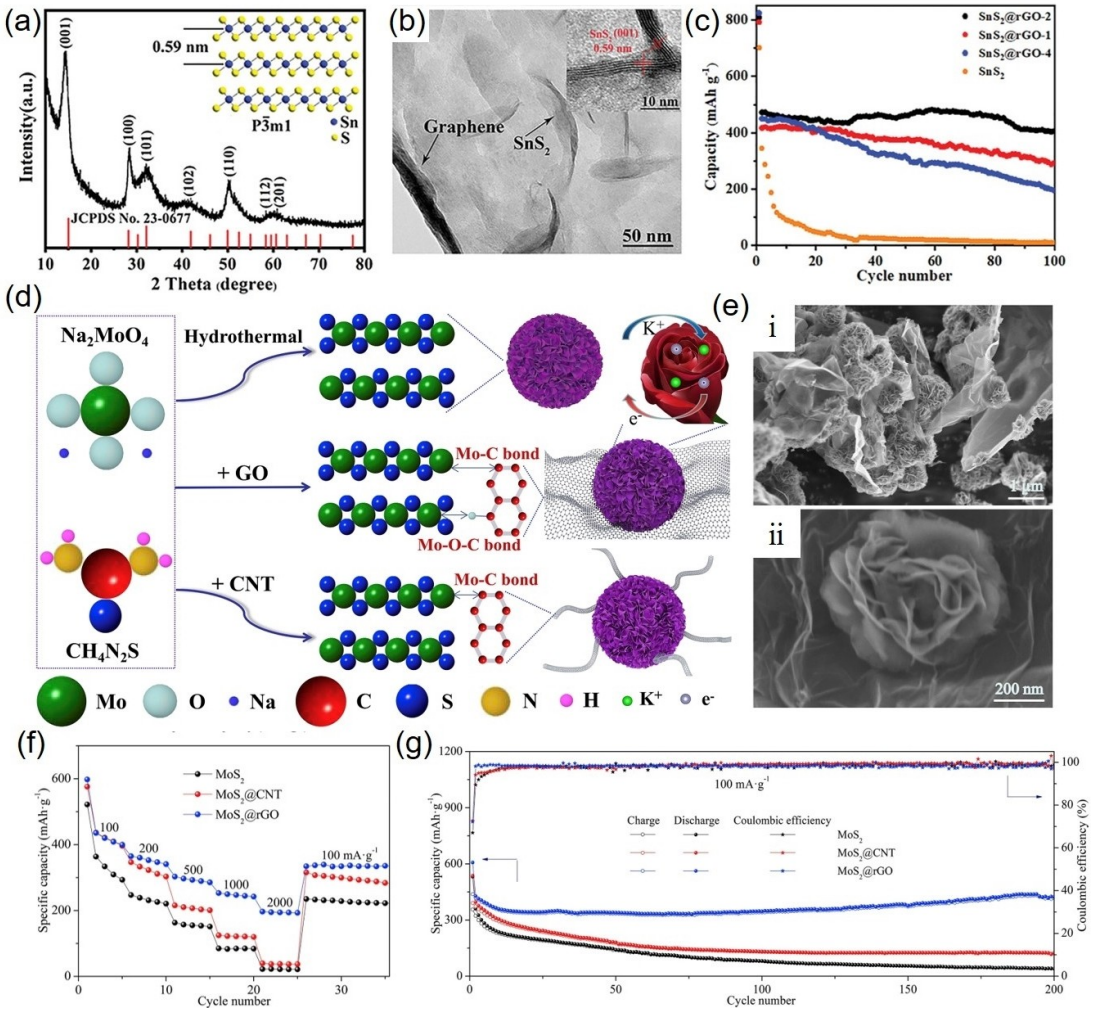

Figure 8. Carbon/conversion anode material composites. a) X-ray diffraction pattern of SnS_2/rGO. b) TEM image of SnS_2/rGO. c) Comparison of cycle performance of SnS_2/rGO and SnS_2 at 0.05 A/g.[31a] Reproduced Ref. [31a] with permission. Copyright (2019) Wiley-VCH. d) MoS_2/carbon composite synthesis process schematic diagram. e) TEM images of MoS_2/rGO at different resolutions. Comparison of (f) rate performance and (g) cycle performance between MoS_2 and corresponding composites.[77] Reproduced Ref. [77] with permission. Copyright (2019) Elsevier.

properties become successful host candidates for other anode materials. They can improve the electrochemical stability of these two types of anodes from two aspects. One is to improve the charge transfer speed of the material as a good conductor or conductive framework of electrons. The other is to serve as a good buffering matrix to withstand volume expansion caused by multiple cycles.

6. Full Cell

Based on the low-cost and high chemical stability, carbon-based materials are the most promising materials for commercialization. The fabrication of full cell is the crucial part to achieve practical application.[78] For full KIBs, the design of anode needs to meet the requirements of be non-toxicity and high capacity.[2] The carbon-based anode can satisfy these features. Currently, some attempts for full KIBs have been reported, where the most popular cathode material are Prussian blue analogue (PBA) and PTCDA. Chen et al. firstly reported PTCDA cathode delivered a high reversible capacity of 130 mAh/g.[42a] Although the cycle stability of PTCDA is outstanding, the discharge plateau (2.2 V and 2.4 V) is low, as shown in Figure 9a.[42a] In addition, owing to the absence of K sources, PTCDA cathode need to pre-inserted potassium. In comparison, PBA cathode with high plateau has more potential to match full KIBs (Figure 9b). Moyer et al. demonstrated the PBA/Graphite full cell with 60% capacity retention (about 25 mAh/g) after 2000 cycles at 2 A/g in 1 M KPF_6 DEGDME.[79] With the optimization of electrolyte, Komaba et al. reported the PBA/graphite full KIBs with superior capacity of 104 mAh/g (based on the weight of cathode) in 7 mol/kg KFSI electrolyte. The full KIBs achieved the high capacity retention of 85% after 101 cycles, as shown in Figure 9c.[59b] Furthermore, binary-salt electrolytes were also developed to combine the advantages of different salts, such as the passivation effect of KPF_6 on the aluminum current collector and KFSI-induced robust SEI. The PBA/graphite full KIBs with KPF_6-KFSI electrolyte (1 mol/kg

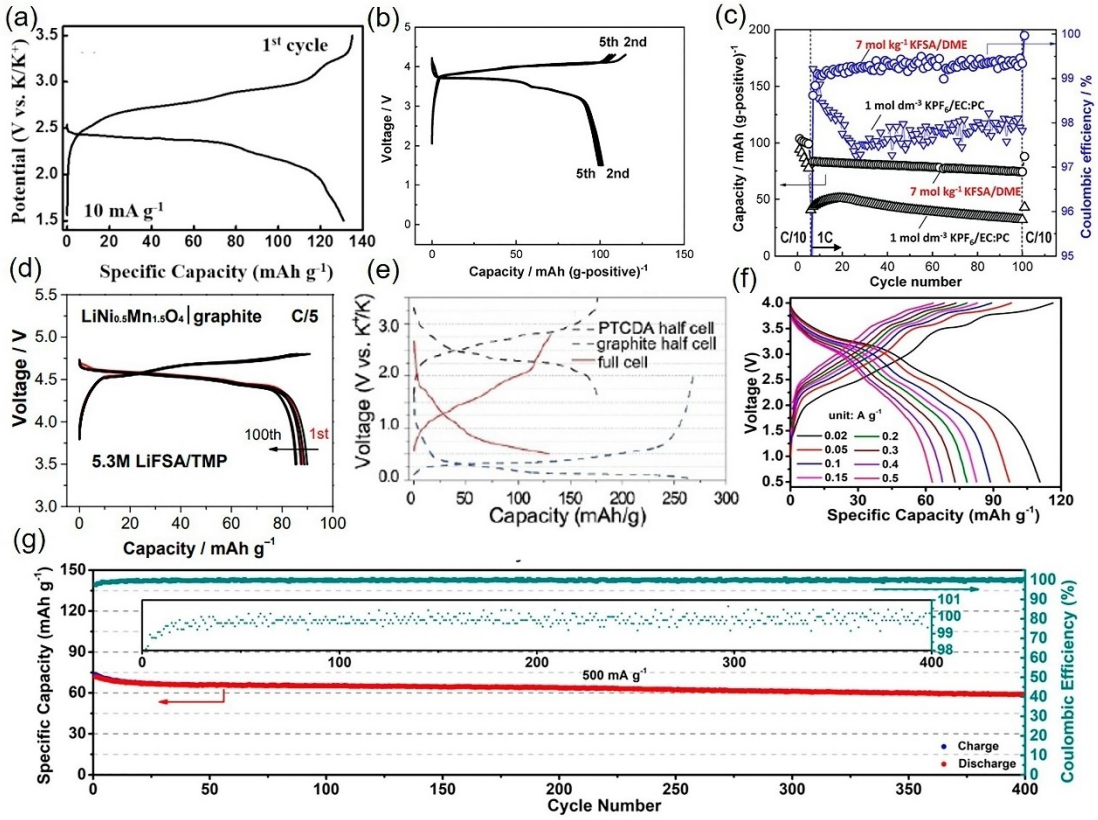

Figure 9. The fabrication of full cell. a) GCD curves of PTCDA cathode for the first cycle at 10 mA/g.[42a] Reproduced from Ref. [42a] with permission. Copyright (2015) Elsevier. b) GCD curves and c) cycle stability of $K_2Mn[Fe(CN)_6]$/graphite full cell using 7 mol/kg KFSI/DME electrolyte.[59b] Reproduced from Ref. [59b] with permission. Copyright (2018) The Royal Society of Chemistry. d) GCD curves for $LiNi_{0.5}Mn_{1.5}O_4$/graphite full cell in 5.3 M LiFSI-TMP electrolyte.[82] Reproduced from Ref. [82] with permission. Copyright (2018) Springer Nature. e) GCD profiles of PTCDA half-cell, graphite half-cell and PTCDA/graphite full cell.[83] Reproduced from Ref. [83] with permission. Copyright (2019) Wiley-VCH. f) GCD profiles and g) cycle stability of $K_{0.5}MnO_2$/graphite full cell.[84] Reproduced from Ref. [84] with permission. Copyright (2020) American Chemical Society.

$K(PF_6)_{0.75}(FSI)_{0.25}$ in EC/PC) maintained 75% capacity after 500 cycles, showing the high K^+ conductivity of the binary-salt electrolyte.[80] The addition of KFSI suppressed PF_6^- decomposition, resulting in the superior SEI, thus the full cell delivered the high ICE of 72.5%.

The fabricating of the full battery requires the optimization and matching of cathode and anode materials, electrolytes, etc. Most of the current electrolytes are not favorable to match the full KIBs. For example, the ICE of traditional ester electrolyte is low, causing the waste of active materials for full cell. The graphite anode suffered the fast capacity decay paired with the traditional ester electrolyte. In addition, the ether electrolyte exhibited the poor high voltage stability,[81] and the high voltage platform of the ternary K-GICs formed by the co-intercalation of K^+ and solvent induced the decrease of the energy density of full KIBs. Therefore, it is urgent to develop wide voltage window electrolyte for full cell, especially for the high voltage PBA cathode. In LIBs, the high voltage stability of phosphate-based electrolytes have been proven effective, such as trimethyl phosphate (TMP) and triethyl phosphate (TEP). The concentrated electrolyte applied to the $LiNi_{0.5}Mn_{1.5}O_4$/graphite battery even reach to 4.8 V (Figure 9d).[82] The high concentration of $LiN(SO_2F)_2$ (LiFSI) hindered the reduction of the TMP solvent, thus forming the salt-derived inorganic SEI. Similar strategies have recently been successfully applied in KIBs. Guo et al. reported the solvation K^+ cations by TEP in different concentration and demonstrated that 2 M KFSI in TEP electrolyte improved the electrochemical performance significantly. The SEI formed in the moderately concentrated electrolyte was more uniform and robust than the KFSI-based EC/DEC electrolytes, suppressing the decomposition of the solvent.[83] The graphite anode achieved the reversible capacity of 275 mAh/g with 90% capacity retention after 300 cycles. By matching with PTCDA cathode with pre-potassiated graphite, the full cell exhibited the reversible capacity of 127 mAh/g with the ICE of 82% (Figure 9e). Coincidentally, Guo et al. replaced the traditional ester solvent (EC/DEC) with TEP to develop the KFSI-based non-flammable electrolyte.[84] The novel electrolyte delivered the encouraging stability in the $K_{0.5}MnO_2$/graphite full cell, corresponding to the reversible capacity of 110.6 mAh/g with the voltage window from 0.5 V to 4.0 V (Figure 9f). It is worth noting that the full KIBs retained 83% capacity, as shown in Figure 9g. Due to the nonflammable feature, phosphorus-based electrolytes are beneficial to enhance the safety of full KIBs, especially for large-scale energy storage. By regulating the concentration of electrolyte, all TMP solvent molecules were

coordinated with K^+ cations when the KFSI/TMP molar ratio is 3:8, and the decomposition of FSI^- induced the formation of F-rich SEI. Using this TMP electrolyte, the PTCDA/graphite full cell exhibited the capacity of 75 mAh/g after 200 cycles at 20 mA/g.[85] The coupling of the special solvation structure and stable SEI effectively suppressed the electrolyte decomposition during cycles, leading to high cycle stability.

In a word, the research on carbon-based anode materials are mainly on the mechanism of K^+ storage and the optimization of electrochemical performance of half-cell, including cycle stability, reversible capacity and rate performance. The systematic investigations on full cell is relatively fewer.

7. Conclusion and Outlook

This review summarized the significant progress of carbon-based anode in KIBs from the aspects of energy storage mechanism, existing unsolved problems of carbon materials and modified strategies. Carbon-based anodes mainly store K^+ ions through intercalation reactions, but the severe volume expansion could injure the cycle stability. Currently, carbon-based anodes have boosted the storage performance by expanding the interlayer spacing, adjusting pore structure, heteroatom doping modification and constructing a stable solid electrolyte interface. With the in-deep research of carbon-based anode, future progress may be predicted as follows.

(1) Although carbon-based anodes have developed to a certain extent in recent years, there is still a big gap between KIBs and commercial LIBs. This requires researchers to develop more compatible carbon-based anodes with high capacity by structural design, so that KIBs will gradually replace LIBs for large-scale energy storage.
(2) Microstructure regulations are considered to be the most practical strategies to protect the stability of carbon-based anode. However, the suitable interlayer spacing for K^+ ions intercalation needs to be further explored, and the regulation of the interlayer spacing also needs to be further controlled. Furthermore, the pore structure increases the K^+ ions adsorption capacity, it also forms a complex SEI to reduce the Coulombic efficiency. The balance between these two aspects needs further exploration.
(3) N-doping carbon-based anodes display high reversible capacity and cycle stability, so it is urgent to exploit the relationship of N-doping and intercalated K^+ ions. That is helpful in understanding the storage mechanism of N-doping carbon anodes, which may bring more effective N-doping structures and process.
(4) Since the composition of SEI plays a decisive role in the cycle stability of carbon-based anode, the formation process in different electrolytes needs to be further studied. At the same time, it is necessary to explore new electrolyte additives to promote the stability of the electrolyte, realizing the control of SEI composition.
(5) The role of carbon-based materials as other types anode host should not be underestimated. The introduction of carbon-based materials into the anodes with severe volume expansion may impressively enhance their cycle stability. However, on account of the low density and small capacity contribution of carbon materials, it is necessary to grasp the content of carbon carriers avoiding the reduction of energy density.
(6) Graphite, as the anode of industrialized LIBs, has the huge application prospect in KIBs. In order to achieve the commercialization of KIBs, the fabrication of full cell requires the superior stability and high Coulombic efficiency of anode. Given the above considerations, great efforts should be made to develop the practical application of modified graphite anode and the suitable ester electrolyte in the future.

Acknowledgements

This work was supported by the National Natural Science Foundation of China (No. 51772167 and 52072206), Local Innovative and Research Teams Project of Guangdong Pearl River Talents Program (2017BT01 N111) and Shenzhen Basic Research Project (Nos. JCYJ20170412171311288, and JCYJ20170817162443934).

Conflict of Interest

The authors declare no conflict of interest.

Keywords: carbon-based anodes · modified strategies · stability · potassium-ion batteries

[1] a) B. Dunn, H. Kamath, J.-M Tarascon, *Science* **2015**, *334*, 928–935; b) K. Lin, Q. Chen, M. R. Gerhardt, L. Tong, S. B. Kim, L. Eisenach, A. W. Valle, D. Hardee, R. G. Gordon, M. J. Aziz, *Science*, **2015**, *349*, 1529–1532.
[2] L. Jiang, Y. Lu, C. Zhao, L. Liu, J. Zhang, Q. Zhang, X. Shen, J. Zhao, X. Yu, H. Li, X. Huang, L. Chen, Y.-S. Hu, *Nat. Energy* **2019**, *4*, 495–503.
[3] a) C. Y. Wang, G. Zhang, S. Ge, T. Xu, Y. Ji, X. G. Yang, Y. Leng, *Nature* **2016**, *529*, 515–518; b) K. H. Park, B. G. Kim, S. H. Song, *Nanomaterials* **2019**, *10*, 1–8; c) Y. Hamon, T. Brousse, F. Jousse, P. Topart, P. Buvat, D. M. Schleich, *J. Power Sources* **2001**, *97–98*, 185–187.
[4] T. C. Wanger, *Conserv. Lett.* **2011**, *4*, 202–206.
[5] J. C. Pramudita, D. Sehrawat, D. Goonetilleke, N. Sharma, *Adv. Energy Mater.* **2017**, *7*, 1602911.
[6] a) Y. Wang, Z. Wang, Y. Chen, H. Zhang, M. Yousaf, H. Wu, M. Zou, A. Cao, R. P. S. Han, *Adv. Mater.* **2018**, *30*, 1802074; b) R. A. Adams, A. Varma, V. G. Pol, *Adv. Energy Mater.* **2019**, *9*, 1900550.
[7] X. Wu, Y. Chen, Z. Xing, C. W. K. Lam, S. S. Pang, W. Zhang, Z. Ju, *Adv. Energy Mater.* **2019**, *9*, 1900343.
[8] a) Z. Jian, Z. Xing, C. Bommier, Z. Li, X. Ji, *Adv. Energy Mater.* **2016**, *6*, 1501874; b) R. Rajagopalan, Y. Tang, X. Ji, C. Jia, H. Wang, *Adv. Funct. Mater.* **2020**, *30*, 1909486; c) Z. Jian, W. Luo, X. Ji, *J. Am. Chem. Soc.* **2015**, *137*, 11566–11569.
[9] a) Y. Xu, C. Zhang, M. Zhou, Q. Fu, C. Zhao, M. Wu, Y. Lei, *Nat. Commun.* **2018**, *9*, 1720; b) D. Su, A. McDonagh, S. Z. Qiao, G. Wang, *Adv. Mater.* **2017**, *29*, 1–8.
[10] Y. N. Ko, S. H. Choi, H. Kim, H. J. Kim, *ACS Appl. Mater. Interfaces* **2019**, *11*, 27973–27981.
[11] a) L. Wang, J. Yang, J. Li, T. Chen, S. Chen, Z. Wu, J. Qiu, B. Wang, P. Gao, X. Niu, H. Li, *J. Power Sources* **2019**, *409*, 24–30; b) K. Kubota, M. Dahbi, T. Hosaka, S. Kumakura, S. Komaba, *Chem. Rev.* **2018**, *18*, 459–479.

[12] T. Hosaka, K. Kubota, A. S. Hameed, S. Komaba, *Chem. Rev.* **2020**, *120*, 6358–6466.
[13] a) W. Yang, J. Zhou, S. Wang, Z. Wang, F. Lv, W. Zhang, W. Zhang, Q. Sun, S. Guo, *ACS Energy Lett.* **2020**, *5*, 1653–1661; b) D. Zhang, Z. Chen, J. Bai, C. Yang, Q. Jiang, *Batteries Supercaps* **2020**, *3*, 185–193.
[14] H. Huang, R. Xu, Y. Feng, S. Zeng, Y. Jiang, H. Wang, Wei Luo, Y. Yu, *Adv. Mater.* **2020**, *32*, 1904320.
[15] a) Y. Wu, S. Hu, R. Xu, J. Wang, Z. Peng, Q. Zhang, Y. Yu, *Nano Lett.* **2019**, *19*, 1351–1358; b) S. Peng, L. Wang, Z. Zhu, K. Han, *J. Phy. Chem. Solids* **2020**, *138*.
[16] J. Zhao, X. Zou, Y. Zhu, Y. Xu, C. Wang, *Adv. Funct. Mater.* **2016**, *26*, 8103–8110.
[17] a) Z. Ju, S. Zhang, Z. Xing, Q. Zhuang, Y. Qiang, Y. Qian, *ACS Appl. Mater. Interfaces* **2016**, *8*, 20682–20690; b) L. Chen, J. Deng, S. Hong, H. Lian, *J. Colloid Interface Sci.* **2020**, *565*, 368–377.
[18] a) J. Hu, Y. Xie, M. Yin, Z. Zhang, *J. Energy Chem.* **2020**, *49*, 327–334; b) Z. Jian, S. Hwang, Z. Li, A. S. Hernandez, X. Wang, Z. Xing, D. Su, X. Ji, *Adv. Funct. Mater.* **2017**, *27*, 1700324.
[19] L. Liu, Z. Lin, J.-Y. Chane-Ching, H. Shao, P.-L. Taberna, P. Simon, *Energy Storage Mater.* **2019**, *19*, 306–313.
[20] a) J. Li, Y. Li, X. Ma, K. Zhang, J. Hu, C. Yang, M. Liu, *Chem. Eng. J.* **2020**, *384*, 123328; b) H. He, D Huang, Y. Tang, Q. Wang, X. Ji, H. Wang, Z. Guo, *Nano Energy* **2019**, 57, 728–736.
[21] Y. Lei, D. Han, J. Dong, L. Qin, X. Li, D. Zhai, B. Li, Y. Wu, F. Kang, *Energy Storage Mater.* **2020**, *24*, 319–328.
[22] X. Wu, D. P. Leonard, X. Ji, *Chem. Mater.* **2017**, *29*, 5031–5042.
[23] a) H. Wang, Z. Xing, Z. Hu, Y. Zhang, Y. Hu, Y. Sun, Z. Ju, Q. Zhuang, *Appl. Mater. Today* **2019**, *15*, 58–66; b) J. Xie, Y. Zhu, N. Zhuang, H. Lei, W. Zhu, Y. Fu, M. S. Javed, J. Li, W. Mai, *Nanoscale* **2018**, *10*, 17092–17098.
[24] W. Luo, J. Wan, B. Ozdemir, W. Bao, Y. Chen, J. Dai, H. Lin, Y. Xu, F. Gu, V. Barone, L. Hu, *Nano Lett.* **2015**, *15*, 7671–7677.
[25] L. Qin, N. Xiao, J. Zheng, Y. Lei, D. Zhai, Y. Wu, *Adv. Energy Mater.* **2019**, *9*, 1902618.
[26] Y. Chen, L. Qin, Y. Lei, X. Li, J. Dong, D. Zhai, B. Li, F. Kang, *ACS Appl. Mater. Interfaces* **2019**, *11*, 45578–45585.
[27] K. Song, C. Cui, L. Mi, S. Chou, W. Chen, C. Shen, *Small* **2019**, 1903194.
[28] W. D. McCulloch, X. Ren, M. Yu, Z. Huang, Y. Wu, *ACS Appl. Mater. Interfaces* **2015**, *7*, 26158–26166.
[29] J. Zheng, Y. Yang, X. Fan, G. Ji, X. Ji, H. Wang, S. Hou, M. R. Zachariah, C. Wang, *Energy Environ. Sci.* **2019**, *12*, 615–623.
[30] K. Xie, K. Yuan, X. Li, W. Lu, C. Shen, C. Liang, R. Vajtai, P. Ajayan, B. Wei, *Small* **2017**, *13*, 1701471.
[31] a) L. Fang, J. Xu, S. Sun, B. Lin, Q. Guo, D. Luo, H. Xia, *Small* **2019**, *15*, e1804806; b) J.-W. Seo, J.-T. Jang, S.-W. Park, C. Kim, B. Park, J. Cheon, *Adv. Mater.* **2008**, *20*, 4269–4273.
[32] J. Yang, Z. Ju, Y. Jiang, Z. Xing, B. Xi, J. Feng, S. Xiong, *Adv. Mater.* **2018**, *30*, 1700104.
[33] a) Y. Tang, J. Zhu, C. Yang, F. Wang, *J. Alloys Compd.* **2016**, *685*, 194–201; b) T. Brezesinski, J. Wang, S. H. Tolbert, B. Dunn, *Nat. Mater.* **2010**, *9*, 146–151.
[34] A. J. Naylor, M. Carboni, M. Valvo, R. Younesi, *ACS Appl. Mater. Interfaces* **2019**, *11*, 45636–45645.
[35] Y. Wen, K. He, Y. Zhu, F. Han, Y. Xu, I. Matsuda, Y. Ishii, J. Cumings, C. Wang, *Nat. Commun.* **2014**, *5*, 4033.
[36] L. Li, W. Zhang, X. Zhang, S. Zhang, Y. Liu, M. Li, G. Zhu, Y. Zheng, Q. Zhang, T. Zhou, W. K. Pang, W. Luo, Z. Guo, J. Yang, *ACS Nano* **2019**, *13*, 7939–7948.
[37] B. Key, R. Bhattacharyya, M. Morcrette, V. Seznec, J.-M. Tarascon, C. O. Grey, *J. Am. Chem. Soc.* **2009**, *131*, 9239–9249.
[38] W. Zhang, Y. Yan, Z. Xie, Y. Yang, Y. Xiao, M. Zheng, H. Hu, H. Dong, Y. Liu, Y. Liang, *J. Colloid Interface Sci.* **2020**, *561*, 195–202.
[39] D. Liu, Z. Yang, W. Li, S. Qiu, Y. Luo, *Electrochim. Acta* **2010**, *55*, 1013–1018.
[40] D. E. Nixon, G. S. Parry, *J. Appl. Phys.* **1968**, *1*, 291–298.
[41] Y. Liu, Y. X. Lu, Y. S. Xu, Q. S. Meng, J. C. Gao, Y. G. Sun, Y. S. Hu, B. B. Chang, C. T. Liu, A. M. Cao, *Adv. Mater.* **2020**, *32*, e2000505.
[42] a) Y. Chen, W. Luo, M. Carter, L. Zhou, J. Dai, K. Fu, S. Lacey, T. Li, J. Wan, X. Han, Y. Bao, L. Hu, *Nano Energy* **2015**, *18*, 205–211; b) W. Li, Z. Li, C. Zhang, W. Liu, C. Han, B. Yan, S. An, X. Qiu, *Solid State Ionics* **2020**, *351*, 115319.
[43] C. Chen, M. Wu, Y. Wang, K. Zaghib, *J. Power Sources* **2019**, *444*, 227310.
[44] W. Wang, J. Zhou, Z. Wang, L. Zhao, P. Li, Y. Yang, C. Yang, H. Huang, S. Guo, *Adv. Energy Mater.* **2018**, *8*, 1701648.
[45] Y. An, H. Fei, G. Zeng, L. Ci, B. Xi, S. Xiong, J. Feng, *J. Power Sources* **2018**, *378*, 66–72.
[46] Z. Tai, Q. Zhang, Y. Liu, H. Liu, S. Dou, *Carbon* **2017**, *123*, 54–61.
[47] Y. Wang, X. Gao, L. Li, M. Wang, J. Shui, M. Xu, *Nano Energy* **2020**, *67*, 104248. [48] a) G. Wang, X. Xiong, D. Xie, Z. Lin, J. Zheng, F. Zheng, Y. Li, Y. Liu, C. Yang, M. Liu, *J. Mater. Chem. A* **2018**, *6*, 24317–24323; b) X. Wu, C. W. K. Lam, N. Wu, S.-S. Pang, Z. Xing, W. Zhang, Z. Ju, *Mater. Today Energy* **2019**, *11*, 182–191.
[48] a) G. Wang, X. Xiong, D. Xie, Z. Lin, J. Zheng, F. Zheng, Y. Li, Y. Liu, C. Yang, M. Liu, *J. Mater. Chem. A* **2018**, *6*, 24317–24323; b) X. Wu, C. W. K. Lam, N. Wu, S.-S. Pang, Z. Xing, W. Zhang, Z. Ju, *Mater. Today Energy* **2019**, *11*, 182–191.
[49] X. S. Tao, Y. G. Sun, Y. Liu, B. B. Chang, C. T. Liu, Y. S. Xu, X. C. Yang, A. M. Cao, *ACS Appl. Mater. Interfaces* **2020**, *12*, 13182–13188.
[50] a) Z. Fan, Y. Wang, Z. Xie, X. Xu, Y. Yuan, Z. Cheng, Y. Liu, *Nanoscale* **2018**, *10*, 9642–9652; b) C. Liu, N. Xiao, H. Li, Q. Dong, Y. Wang, H. Li, S. Wang, X. Zhang, J. Qiu, *Chem. Eng. J.* **2020**, *382*, 121759; c) M. Chen, W. Wang, X. Liang, S. Gong, J. Liu, Q. Wang, S. Guo, H. Yang, *Adv. Energy Mater.* **2018**, *8*, 1800171.
[51] Z. Sheng, L. Shao, J. Chen, W. Bao, F. Wang, X. Xia, *ACS Nano* **2011**, *5*, 4350–4358.
[52] F. Zheng, Y. Yang, Q. Chen, *Nat. Commun.* **2014**, *5*, 5261.
[53] a) P. Li, J.-Y. Hwang, Y.-K. Sun, *J. Mater. Chem. A* **2019**, *7*, 20675–20682; b) Y. An, Y. Tian, Y. Li, S. Xiong, G. Zhao, J. Feng, Y. Qian, *J. Mater. Chem. A* **2019**, *7*, 21966–21975.
[54] R. C. Cui, B. Xu, H. J. Dong, C. C. Yang, Q. Jiang, *Adv. Sci.* **2020**, 1902547.
[55] L. Wang, J. Jia, Y. Wu, K. Niu, *J. Appl. Electrochem.* **2018**, *48*, 1115–1120.
[56] L. Fan, S. Chen, R. Ma, J. Wang, L. Wang, Q. Zhang, E. Zhang, Z. Liu, B. Lu, *Small* **2018**, *14*, e1801806.
[57] L. Fan, R. Ma, Q. Zhang, X. Jia, B. Lu, *Angew. Chem. Int. Ed.* **2019**, *58*, 10500–10505.
[58] H. J. Kim, N. Voronina, H. Yashiro, S. T. Myung, *ACS Appl. Mater. Interfaces* **2020**.
[59] a) Y. Yamada, C. H. Chiang, K. Sodeyama, J. Wang, Y. Tateyama, A. Yamada, *ChemElectroChem* **2015**, *2*, 1687–1694; b) T. Hosaka, K. Kubota, H. Kojima, S. Komaba, *Chem. Commun.* **2018**, *54*, 8387–8390; c) H.-B. Han, S.-S. Zhou, D.-J. Zhang, S.-W. Feng, L.-F. Li, K. Liu, W.-F. Feng, J. Nie, H. Li, X.-J. Huang, *J. Power Sources* **2011**, *196*, 3623–3632.
[60] P. Münster, A. Heckmann, R. Nölle, M. Winter, K. Beltrop, T. Placke, *Batteries Supercaps* **2019**, *2*, 992–1006.
[61] a) E. Zhang, X. Jia, B. Wang, J. Wang, X. Yu, B. Lu, *Adv. Sci.* **2020**, 2000470; b) W. Zhang, Z. Wu, J. Zhang, G. Liu, N.-H. Yang, R.-S. Liu, W. K. Pang, W. Li, Z. Guo, *Nano Energy* **2018**, *53*, 967–974; c) N. Xiao, W. D. McCulloch, Y. Wu, *J. Am. Chem. Soc.* **2017**, *139*, 9475–9478; d) W. Zhang, W. K. Pang, V. Sencadas, Z. Guo, *Joule* **2018**, *2*, 1534–1547.
[62] H. Wang, H. Wang, S. Chen, B. Zhang, G. Yang, P. Gao, J. Liu, X. Fan, Y. Huang, J. Lin, Z. Shen, *ACS Appl. Energ. Mater.* **2019**, *2*, 7942–7951.
[63] Y. Jin, N. H. Kneusels, C. P. Grey, *J. Phys. Chem. Lett.* **2019**, *10*, 6345–6350.
[64] Y. Lei, L. Qin, R. Liu, K. C. Lau, Y. Wu, D. Zhai, B. Li, F. Kang, *ACS Appl. Energ. Mater.* **2018**, *1*, 1828–1833.
[65] Y. Liu, D. Lin, Y. Li, G. Chen, A. Pei, O. Nix, Y. Li, Y. Cui, *Nat. Commun.* **2018**, *9*, 3656.
[66] X. Bie, K. Kubota, T. Hosaka, K. Chihara, S. Komaba, *J. Mater. Chem. A* **2017**, *5*, 4325–4330.
[67] J. Liao, Q. Hu, Y. Yu, H. Wang, Z. Tang, Z. Wen, C. Chen, *J. Mater. Chem. A* **2017**, *5*, 19017–19024.
[68] J. Dong, Y. Lei, D. Han, H. Wang, D. Zhai, B. Li, F. Kang, *Chem. Commun.* **2019**, *55*, 12555–12558.
[69] J. Xie, X. Li, H. Lai, Z. Zhao, J. Li, W. Zhang, W. Xie, Y. Liu, W. Mai, *Angew. Chem. Int. Ed.* **2019**, *58*, 14740–14747.
[70] H. Wang, D. Zhai, F. Kang, *Energy Environ. Sci.* **2020**, *13*, 4583–4608.
[71] V. Gabaudan, R. Berthelot, M. T. Sougrati, P.-E. Lippens, L. Monconduit, L. Stievano, *J. Mater. Chem. A* **2019**, *7*, 15262–15270.
[72] Q. Zhang, J. Mao, W. K. Pang, T. Zheng, V. Sencadas, Y. Chen, Y. Liu, Z. Guo, *Adv. Energy Mater.* **2018**, *8*, 1703288.
[73] N. M. Caffrey, *Nanoscale* **2018**, *10*, 13520–13530.
[74] Y. Wu, H. B. Huang, Y. Feng, Z. S. Wu, Y. Yu, *Adv. Mater.* **2019**, *31*, 1901414.
[75] a) S. Di, P. Ding, Y. Wang, Y. Wu, J. Deng, L. Jia, Y. Li, *Nano Res.* **2020**, *13*, 225–230; b) J. Wang, B. Wang, Z. Liu, L. Fan, Q. Zhang, H. Ding, L. Wang, H. Yang, X. Yu, B. Lu, *Adv. Sci.* **2019**, *6*, 1900904; c) F. Han, S. Luo, L. Xie, J. Zhu, W. Wei, X. Chen, F. Liu, W. Chen, J. Zhao, L. Dong, K. Yu, X. Zeng, F. Rao, L. Wang, Y. Huang, *ACS Appl. Mater. Interfaces* **2019**, *11*, 8443–8452.

[76] J. Ge, L. Fan, J. Wang, Q. Zhang, Z. Liu, E. Zhang, Q. liu, X. Yu, B. Lu, *Adv. Energy Mater.* **2018**, *8*, 1801477.
[77] S. Chong, L. Sun, C. Shu, S. Guo, Y. Liu, W. Wang, H. K. Liu, *Nano Energy* **2019**, *63*, 103868.
[78] W. Zhang, Y. Liu, Z. Guo, *Sci. Adv.* **2019**, *5*, 1–13.
[79] K. Moyer, J. Donohue, N. Ramanna, A. P. Cohn, N. Muralidharan, J. Eaves, C. L. Pint, *Nanoscale* **2018**, *10*, 13335–13342.
[80] T. Hosaka, T. Matsuyama, K. Kubota, S. Yasuno, S. Komaba, *ACS Appl. Mater. Interfaces* **2020**, *12*, 34873–34881.
[81] K. Lei, Z. Zhu, Z. Yin, P. Yan, F. Li, J. Chen, *Chem* **2019**, *5*, 3220–3231.
[82] J. Wang, Y. Yamada, K. Sodeyama, E. Watanabe, K. Takada, Y. Tateyama, A. Yamada, *Nat. Energy* **2017**, *3*, 22–29.
[83] S. Liu, J. Mao, Q. Zhang, Z. Wang, W. K. Pang, L. Zhang, A. Du, V. Sencadas, W. Zhang, Z. Guo, *Angew. Chem. Int. Ed.* **2020**, *59*, 3638–3644.
[84] L. Deng, T. Wang, Y. Hong, M. Feng, R. Wang, J. Zhang, Q. Zhang, J. Wang, L. Zeng, Y. Zhu, L. Guo, *ACS Energy Lett.* **2020**, *5*, 1916–1922.
[85] S. Liu, J. Mao, L. Zhang, W. K. Pang, A. Du, Z. Guo, *Adv. Mater.* **2020**, 2006313.

Manuscript received: October 9, 2020
Revised manuscript received: December 6, 2020
Version of record online: December 29, 2020